Journal of Biomedical Optics

BiomedicalOptics.SPIEDigitalLibrary.org

Pressure injury prediction using diffusely scattered light

David Diaz
Alec Lafontant
Michael Neidrauer
Michael S. Weingarten
Rose Ann DiMaria-Ghalili
Ericka Scruggs
Julianne Rece
Guy W. Fried
Vladimir L. Kuzmin
Leonid Zubkov

SPIE.

David Diaz, Alec Lafontant, Michael Neidrauer, Michael S. Weingarten, Rose Ann DiMaria-Ghalili, Ericka Scruggs, Julianne Rece, Guy W. Fried, Vladimir L. Kuzmin, Leonid Zubkov, "Pressure injury prediction using diffusely scattered light," *J. Biomed. Opt.* **22**(2), 025003 (2017), doi: 10.1117/1.JBO.22.2.025003.

Journal of Biomedical Optics 22(2), 025003 (February 2017)

Pressure injury prediction using diffusely scattered light

David Diaz,[a] Alec Lafontant,[a] Michael Neidrauer,[a] Michael S. Weingarten,[b] Rose Ann DiMaria-Ghalili,[c] Ericka Scruggs,[d] Julianne Rece,[d] Guy W. Fried,[d] Vladimir L. Kuzmin,[e] and Leonid Zubkov[a,*]
[a]Drexel University, School of Biomedical Engineering, Philadelphia, Pennsylvania, United States
[b]Drexel University, College of Medicine, Department of Surgery, Philadelphia, Pennsylvania, United States
[c]Drexel University, College of Nursing and Health Professions, Philadelphia, Pennsylvania, United States
[d]Magee Rehabilitation Hospital, Philadelphia, Pennsylvania, United States
[e]St. Petersburg Polytechnic University, Saint Petersburg, Russia

Abstract. Pressure injuries (PIs) originate beneath the surface of the skin at the interface between bone and soft tissue. We used diffuse correlation spectroscopy (DCS) and diffuse near-infrared spectroscopy (DNIRS) to predict the development of PIs by measuring dermal and subcutaneous red cell motion and optical absorption and scattering properties in 11 spinal cord injury subjects with only nonbleachable redness in the sacrococcygeal area in a rehabilitation hospital and 20 healthy volunteers. A custom optical probe was developed to obtain continuous DCS and DNIRS data from sacrococcygeal tissue while the subjects were placed in supine and lateral positions to apply pressure from body weight and to release pressure, respectively. Rehabilitation patients were measured up to four times over a two-week period. Three rehabilitation patients developed open PIs (POs) within four weeks and eight patients did not (PNOs). Temporal correlation functions in the area of redness were significantly different ($p < 0.01$) during both baseline and applied pressure stages for POs and PNOs. The results show that our optical method may be used for the early prediction of ulcer progression. © *2017 Society of Photo-Optical Instrumentation Engineers (SPIE)* [DOI: 10.1117/1.JBO.22.2.025003]

Keywords: diffuse correlation spectroscopy; mobility; pressure injuries.

Paper 160543RR received Aug. 8, 2016; accepted for publication Jan. 23, 2017; published online Feb. 11, 2017.

1 Introduction

Diffuse correlation spectroscopy (DCS) and diffuse near-infrared spectroscopy (DNIRS) are two methods that measure diffusely scattered light in human tissue and are now widely used in medical research diagnostic applications. The main applications of these technologies are in the detection and monitoring of breast cancer tumors during therapy and neurological conditions, such as the degree of brain injury following a stroke, sleep apnea, and brain activations.[1–6] DCS has also been used to study cerebral perfusion in neonates[7–11] in addition to several other various types of cancer, such as head and neck, bone marrow, prostate, and thyroid cancer[12–16] as well as preclinical experimental oncology studies.[17–21]

We have completed several research studies using frequency domain DNIRS studying wound healing in animal models and human diabetic wounds.[22–24] These studies showed that changes over a 3- to 4-week period in the blood saturation and absolute hemoglobin concentration calculated from measured optical absorption coefficient of tissue underlying chronic diabetic wounds can predict 20-week healing outcomes. These data led us to hypothesize that diffuse optical methods can be used to predict the development of a pressure injury (PI) (i.e., pressure ulcers).

2 Current Pressure Ulcer Prediction Methods

The National Pressure Ulcer Advisory Panel (NPUAP) defines PI (formerly called pressure ulceration) as localized damage to the skin and/or underlying soft tissue usually over a bony prominence. Early PI begins with local tissue ischemia, tissue deformation, and local inflammation caused by excessive pressure and/or shear stress in soft tissue near bony prominences leading to tissue destruction.[25,26] The NPUAP defines six categories for classifying PIs: stage 1, 2, 3, and 4 PI, unstageable PI, and deep tissue PI. Stage 1 PIs are characterized by nonblanchable redness, which is often the first sign of PI development. While some cases of redness progress to open PIs, others disappear.

Currently, clinicians assess the risk of PI progression based on surface appearance and palpation and through tools such as the Braden, Norton, and Waterlow scales.[27] Therefore, a quantitative objective method of PI risk assessment would be beneficial for directing initial treatment options, improving patient outcomes, and reducing hospital stays. Early identification of PI may allow clinicians to provide aggressive care at an early stage to avoid further progression.

There have been few studies done to predict the progression of PIs using blood flow monitoring technologies. In 2009, Aoi et al.[28] conducted a study using intermediate-frequency ultrasonography (10 MHz) to evaluate deep tissue injuries (DTIs) (~2 to 3 cm). Among the 12 patients who were analyzed, six of the patients' ulcers worsened compared to initial measurements, while the other half healed. Using the ultrasound analysis, they were able to predict PI progression with a positive predictive value, specificity, and sensitivity greater than 80%.

In 2011, Judy et al.[29] used thermography to evaluate PI development and risk assessment. From 100 adult patients

*Address all correspondence to: Leonid Zubkov, E-mail: laz23@drexel.edu

1083-3668/2017/$25.00 © 2017 SPIE

who were enrolled in the study at Duke University Medical Center over a 1.5-year period, only five participants developed a stage 1 or 2 PI. They developed an algorithm to classify patients based on the risk of developing a pressure ulcer and were able to differentiate between patients who developed an ulcer and those who did not. All of the five patients who developed an advanced PI were classified as high-risk patients, and they determined that the Braden scores correctly identified only three of the five participants who developed a PI to be at high risk of PI development.

3 Material and Methods

3.1 *Human Study*

All procedures involving human subjects were reviewed and approved by the Institutional Review Boards at Magee Rehabilitation Hospital and Drexel University. Participants included 20 healthy subjects (HSs) and 11 rehabilitation (spinal cord injury) patients admitted at Magee Rehabilitation Hospital in Philadelphia.

HSs, 18 years of age or older, with no history of PI, diabetes, venous, or arterial disease were recruited to optimize the measurement protocol, assess feasibility, evaluate ease of use, and compare measured optical parameters in the sacral area to data collected from rehabilitation patients. After the robustness of the device and newly designed probe had been tested, rehabilitation patients were recruited.

Eligible patients had intact sacrococcygeal skin with nonblanchable redness (i.e., either a stage 1 PI or DTI[26]). Patients were ineligible for the study if they suffered from diabetes, venous, or arterial disease or had a previous history of sacrococcygeal stage 2, 3, or 4 PIs.

Table 1 shows demographic information on three rehabilitation patients who developed open PIs (POs) and eight patients who did not develop open ulcers (PNOs).

3.2 *Measurement Protocol*

The measurement protocol shown in Fig. 1 consisted of three stages: baseline, applied pressure, and released pressure. First, during the baseline stage, the subject was moved into a lateral position on a hospital bed and baseline measurements were obtained by gently touching the optical probe to the subject's sacrococcygeal skin for 1 to 2 min. A sterile transparent dressing (Tegaderm, 3M, Corp) was used to cover the probe

Table 1 Demographic information for all enrolled subjects.

ID	Sex	Race	Age	BMI	Braden score	Braden indication	Final stage
PNO1	M	Caucasian	59	23.4	10	High risk	Healed
PNO2	M	Caucasian	20	26.9	11	High risk	Healed
PNO3	F	Caucasian	21	21.6	11	High risk	Healed
PNO4	M	Caucasian	62	37.9	15	At risk	Healed
PNO5	M	Caucasian	52	26.7	12	High risk	Healed
PNO6	M	Caucasian	48	28.4	10	High risk	Healed
PNO7	M	Caucasian	55	39.6	14	Moderate risk	Healed
PNO8	M	Caucasian	50	31.6	15	At risk	Healed
PO1	M	Caucasian	79	19.2	13	Moderate risk	Unstageable
PO2	M	Caucasian	30	22.6	10	High risk	Stage 3
PO3	M	Caucasian	34	20.3	12	High risk	Unstageable

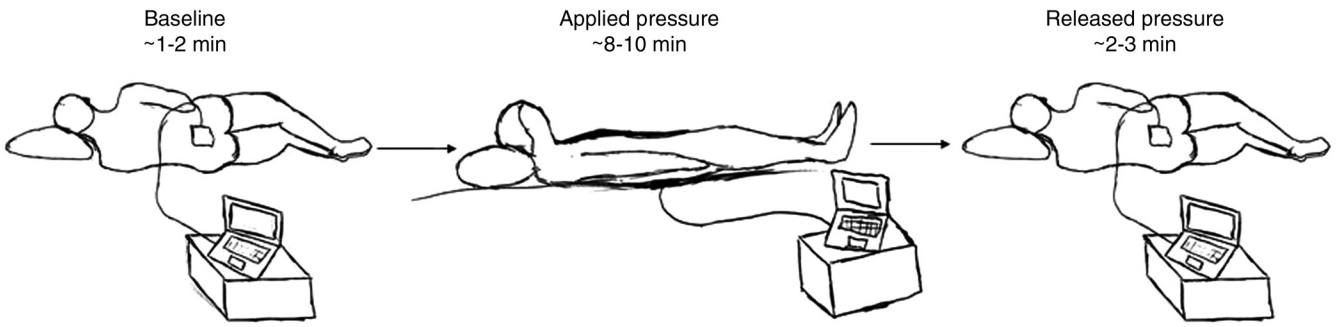

Fig. 1 The three stages of the measurement protocol. The patient begins in the lateral position during the baseline stage, then is moved to the supine position for the applied pressure stage, and finally is moved back to the lateral position to release the pressure.

during each measurement session, in accordance with universal precautions. Next, during the applied pressure stage, the subject was moved into the supine position with body weight applying pressure to the sacral area for 8 to 10 min. This position simulates conditions that may lead to PI development if sustained for a longer period of time. During the last stage of the protocol when the pressure was released, the subject was moved from the supine position back to the lateral position, and optical measurements were continued for another 2 to 3 min similar to baseline measurements. During each stage, the measurement cycle was 6 s, during which DCS correlation functions were measured for 3 s and DNIRS data were obtained for 3 s.

Measurement sessions were performed four times over the course of two weeks or until the patient developed an open PI, which appeared on the skin surface (stage 2, 3, 4, or unstageable PI). Two weeks after the last measurement session, each patient was examined to determine whether an open PI had developed.

3.3 *Diffuse Correlation Spectroscopy Instrumentation*

DCS was used to measure microcirculatory blood flow in potentially damaged sacral tissue. A long-coherent length (~10 m) laser (CrystaLaser, Reno, Nevada) emission traveled through a multimode optical fiber to the tissue. A four-channel single photon counting module (SPCM) (Pacer, Palm Beach Gardens, Florida) registered the scattered light that was brought back from tissue by four single mode fibers (core diameter ~5 μm). The output of the SPCM was connected to a multitau correlator (Correlator.com, Shenzhen, China), which computed a temporal correlation function (TCF) of scattered light intensity selected based on the photon arrival times. This multitau correlator was selected because it analyzes TCF across a wide range of τ (10^{-6} to 10^{-1}), which is necessary because tissue is a multiscattering regime where the characteristic time strongly depends on the number light scattering events.[30–33]

3.4 *Diffuse Near-Infrared Spectroscopy Device*

The frequency domain DNIRS device measures tissue optical properties μ_a and μ_s'. Measured values of μ_a and μ_s' can be used to determine absolute values of blood flow index (BFI) from experimental TCF when the DCS system is operated simultaneously with the DNIRS system in the same tissue volume.

A DNIRS system with two avalanche photodiode detectors and eight multimode (62.5/125 μm) source fibers delivering 160 MHz intensity-modulated light (685 and 830 nm) was used to calculate tissue optical properties. For more details on the DNIRS system, see Ref. 34. An optical switch (Dicon) was used to deliver one wavelength of light to one source fiber at a time. Backscattered light was collected via two detector fibers (1-mm core). Amplitude and phase shift values, as functions of 16 source–detector separations (i.e., eight sources and two detectors), were fit to the diffusion approximation model in semi-infinite geometry, and optical properties were calculated.[35] These μ_a and μ_s' values were used for the calculation of BFI.[30]

To verify the consistency of the DNIRS system throughout the study, we measured the optical properties of a silicone phantom before each measurement session, and variation in calculated μ_a and μ_s' did not exceed 10%. Because our DCS system operates at a wavelength of 785 nm while the DNIRS system operates at 685 and 830 nm, we adjusted the measured values of μ_s' by interpolating between μ_s' measured at 685 and 830 nm. When fitting measured values of scattered light intensity and phase changes, we rejected measurements with root-mean-square deviations between experimental data and fitting were greater than 25%.

3.5 *Optical Probe Design*

To measure the response of sacral tissue to applied pressure, an optical probe was developed. This probe, pictured in Fig. 2, was used for DCS and DNIRS measurements during all three stages of our protocol: baseline, applied pressure, and released pressure.

The probe immobilized and protected the DCS and DNIRS optical fibers by integrating them into a 3-D-printed acrylonitrile butadiene styrene fixture that was embedded within a silicone pad. Ninety deg optical prisms (2 mm per side) were fixed to the ferrule tip of each fiber using optical adhesive that redirects light into the vertical direction when patients are in the supine position with their sacral skin above the silicone pad. The single source–detector separation for DCS fibers was 6 mm, corresponding to a measurement depth of approximately 2 to 5 mm.[36,37] The DNIRS part of the probe has source–detector separations ranging between 6 and 16 mm, corresponding to measurement depths of 2 to 9 mm. We evaluate the penetration depth as the value of order of square root of product of the source–detector distance and $1/\mu_s'$, i.e., $\sqrt{\rho \times 1/\mu_s'}$, where ρ is the source–detector separation. The optical power of light transmitted through the fibers with prisms was approximately 90% of the transmission from the same fibers without prisms. A polarized film was placed in front of DCS detector fibers.

3.6 *Modeling Diffuse Correlation Spectroscopy Data*

Within the diffusion regime of light propagation in a tissue, the field TCF for an infinite medium takes the form[30]

$$G_1(\tau) = r^{-1} \exp(-Kr), \tag{1}$$

where r is the source–detector distance, the square of decay parameter

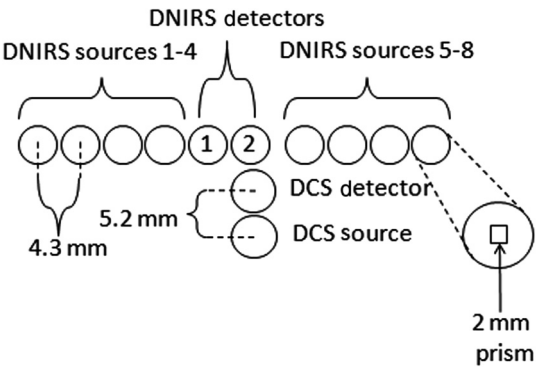

Fig. 2 Schematic drawing of the optical probe used during the human study protocol. Small prisms were fixed onto the ferrals of each fiber to redirect the light 90 deg, so measurements could be taken during all three stages of the protocol. The typical separation between the DNIRS sources is approximately 4.3 mm while the separation between DCS source and detector is about 5.2 mm.

$$K^2 = 3\mu_a\mu_s' + \alpha\mu_s'^2 k^2 \langle \Delta r^2(\tau)\rangle, \quad (2)$$

μ_s' and μ_a are the reduced scattering and adsorption coefficients, $k = 2\pi n/\lambda$, λ is the wavelength, n is the tissue refractive index, and $\langle \Delta r^2(\tau)\rangle$ is the mean square displacement (MSD). Factor α is understood as a share of moving scatterers; the first term is responsible for static light scattering and the second term for dynamic decay of field correlations. For a semi-infinite space, the field TCF is presented within the diffusion solution as a difference between two terms contributed by the radiation source and its mirror image

$$G_1(\tau) = [r_1^{-1}\ \exp(-Kr_1) - r_2^{-1}\ \exp(-Kr_2)], \quad (3)$$

where r_1 and r_2 are the source–detector and source image–detector distances, respectively [see (Ref. 31)].

Beginning with the pioneering works[32,38] on diffusive wave spectroscopy (DWS), the MSD is commonly explained in terms of the Brownian diffusion

$$\langle \Delta r^2(\tau)\rangle_{\text{Brown}} = 6D_b\tau, \quad (4)$$

where D_b is the diffusion coefficient of the red blood cells (RBC) moving in tissue. As is seen, Brownian diffusion exhibits linear dependence on the temporal decay τ.

For numerical evaluation, it is convenient to present the decay parameter K as follows:

$$K = \sqrt{3\mu_a\mu_s'(1 + 2\alpha\mu_a^{-1}\ \mu_s' k^2 D_b\tau)}. \quad (5)$$

Estimating reduced scattering and absorption coefficients $\mu_s' = 10\ \text{cm}^{-1}$ and $\mu_a = 0.1\ \text{cm}^{-1}$, respectively, and taking typical values $k \approx 10\ \mu\text{m}^{-1}$ and $\alpha D_b = 0.510^{-8}\ \text{cm}^2/\text{s}$, we conclude that the second term dominates for delay times exceeding $\tau > 10^{-4}$ s, and we come to a nonanalytic, square-root dependence on time

$$K \approx \mu_s'\sqrt{6\alpha k^2 D_b\tau}. \quad (6)$$

DWS has been studied primarily using this nonanalytic approximation.[32,38] Note that this nonanalyticity makes the N-order method,[39] based on the Taylor expansion method, nonjustified.

For smaller delay times and larger absorption coefficients, the parameter K exhibits a linear dependence on time

$$K = \sqrt{3\mu_a\mu_s'}[1 + \alpha(\mu_s'/\mu_a)k^2 D_b\tau]. \quad (7)$$

Thus, for a chosen set of tissue and light parameters, the temporal behavior of the TCF changes qualitatively, as the time delay increases within the temporal range $10^{-5} < \tau < 10^{-3}$ s, from linear to the square-root dependence. In this case, when the diffusion regime is violated, the time dependence of the TCF also returns to being linear. Such an effect we are to expect for bounded tissue geometries, namely for multilayer systems, soft tissue, and bone as an example, with the layer thickness comparable with the transport length $\mu_s'^{-1}$.

Besides the widely accepted diffusive model of the scatterers dynamics, there has been considered also the random velocity model,[40] wherein the MSD is proportional to the second moment of the velocity

$$\langle \Delta r^2(\tau)\rangle_{\text{convect}} = \langle V^2\rangle\tau^2. \quad (8)$$

While the MSD of Brownian particle increases with time linearly, within in the random velocity model it depends on the square of time. Thus, the Brownian model and the random velocity model predict quite different dynamics of scatterers. Both mechanisms can be considered simultaneously (see Refs. 41 and 42), contributing additively to the MSD.

Using the Brownian model, one takes the RBC diffusion coefficient, multiplied with α, as the index of blood flow, $\text{BFI}_{\text{Browning}} = \alpha D_b$. Within the convective MSD model, the BFI in Ref. 41 is calculated as the root of second moment of velocity, $\text{BFI}_{\text{convect}} = \sqrt{\alpha\langle V^2\rangle}$. Therefore, it is seen that even the dimensions of these quantities are different.

Both models can be considered simultaneously as a mixed model.

In recent work,[42] the Monte Carlo simulations were performed presenting the MSD as the sum of contributions of the convective and diffusive movements of RBCs; in particular, the diffusion coefficient and RBC velocity were calculated using an artificial-specific picture of parallel oriented capillaries with a given radius, optical coefficients of blood and surrounding tissues, and Poiseuille-like velocity profile. However, Boas et al.[42] admit that the experimental data primarily reflect the diffusive character of the RBC dynamics.

Practically, assuming that the velocity profile in a cylindrical blood vessel takes the Poiseuille-like form, Boas et al.[42] have shown for such a detailed model of blood circulatory system that DCS mainly measures RBC shear-induced diffusion. Based on results of the Monte Carlo simulations, the authors found that the BFI, which is shown to quantify tissue perfusion, is linearly proportional to blood flow, dependent on the hemoglobin concentration and blood vessel diameter.

The measured TCF of intensity, $g_2(\tau) = \langle I(r,t) \times I(r,\ t+\tau)\rangle/\langle I(r,t)\rangle^2$, is the quadratic form of the field TCF due to the Siegert relationship

$$g_2(\tau) = 1 + \beta|g_1(\tau)|^2, \quad (9)$$

where $g_1(\tau) = G_1(\tau)/G_1(0)$ is the normalized field TCF. Presently, when calculating the BFI, the measured data are fitted using the diffusion solution for the field TCF in a semi-infinite geometry, typically for the Brownian diffusion. Some less successive fittings are done using the random velocity MSD model, with fittings not as good as the diffusive model.

4 Results

4.1 *Temporal Correlation Functions as Markers for Prediction of Pressure Injury Development*

Representative TCFs, measured by our DCS instrumentation, are shown in Fig. 3. Delay time, τ_{exp}, was calculated from the TCF where the function decreased by a factor of e (mathematical constant $e = 2.72\ldots$) because, according to the theoretical concept, the TCF shape is nearly exponential. The raw TCF curves obtained from POs during baseline measurements had smaller delay τ compared with TCFs of HSs and PNOs.

Detailed results are shown for POs in Fig. 4, in which τ_{exp} values are lower than τ_{exp} for PNOs and HSs.

The ratios of $\tau_{\text{exp .pressure}}$ during applied pressure to $\tau_{\text{exp .baseline}}$ during baseline were calculated and illustrated in Fig. 5. We

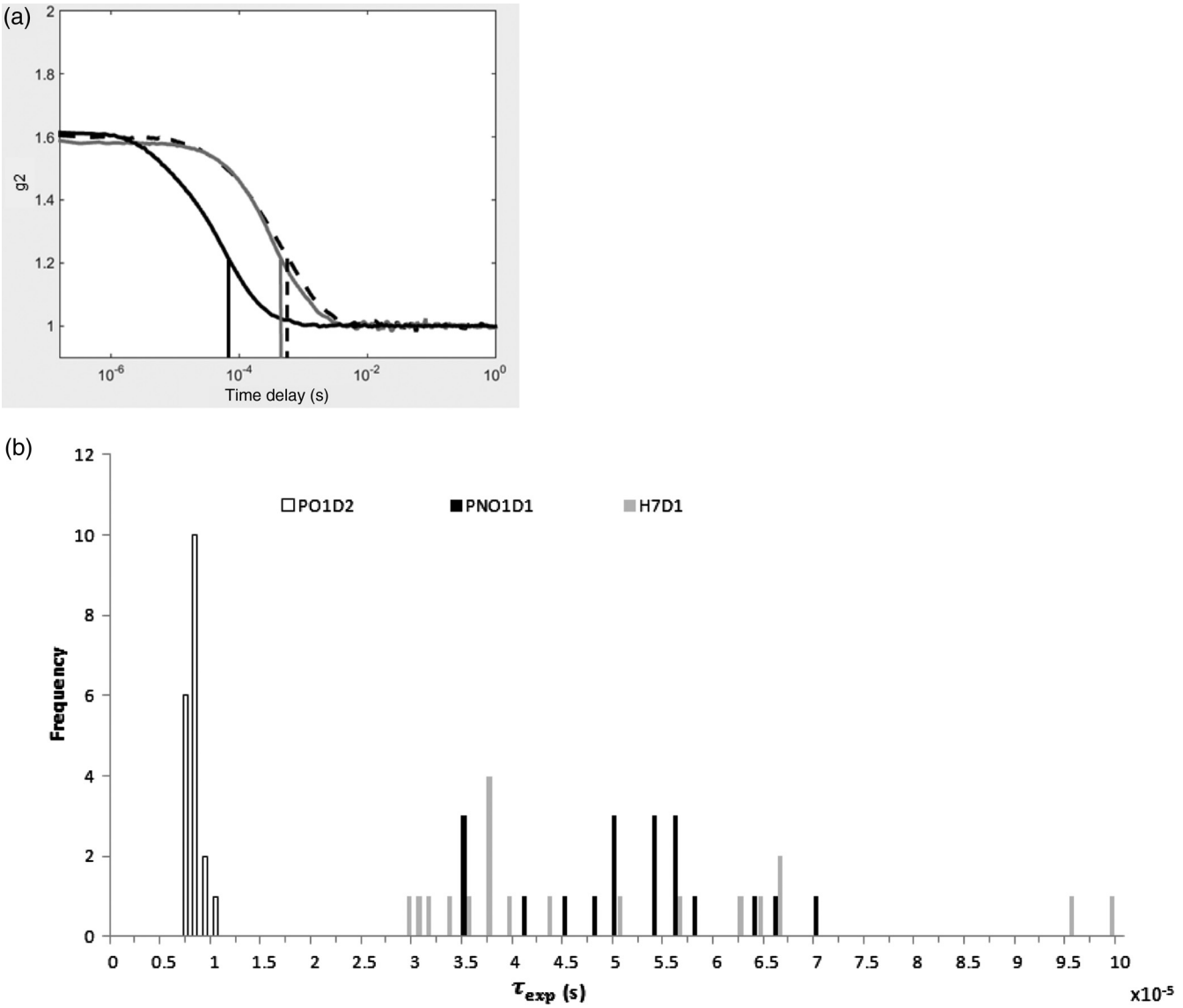

Fig. 3 (a) Typical experimental TCF of intensity for all three groups of patients for baseline. The PO (dark line), PNO (gray line), and healthy volunteers (dotted line). Representative curves were taken from PO1D2, PNO1D1, and HS7D1. Positions of vertical lines indicate the value of τ_{exp}. (b) Histogram of TCFs ($n = 19$) during the baseline stage of one measurement session for PO1D2, PNO1D1, and HS7D1. The registration time of each TCF is ~1.5 s, and the histograms are divided into bin sizes of 10^{-5} s.

observed an increase of about nine times in τ_{exp} when POs were moved to the supine position and pressure was applied to the sacral area, whereas for PNOs and HSs, the increase was only approximately two times.

4.2 *Analysis of Diffuse Near-Infrared Spectroscopy Optical Properties*

The optical properties μ_a and μ_s' in DNIRS measurements are determined from fitting the scattered amplitude and phase change values as function of 16 source–detector separations ρ to the semi-infinite approximation of the diffusion model.[31,43] Using the criteria for data accuracy verification described in Sec. 3.4, 3 of 10 PO and 11 of 28 PNO data points were excluded from this analysis. We suppose that some of these measurements were not stable for two reasons: first, we did not have uniform contact between the skin and the probe due to body curvature in the sacrum area, particularly in the supine position where we cannot adjust the probe under the patient's body. Second, patient motion artifacts (for example muscle spasms) may have contributed to this problem.

Table 2 shows the average μ_a and μ_s' values for each stage and each patient group.

As shown in Sec. 3.6, BFI can be determined using measured values of μ_a, μ_s', and τ_{exp}. Therefore, the changes in τ_{exp} across different stages of our measurement protocol and the differences in τ_{exp} between subjects that we presented above in Sec. 4.1 may be related to changes in the optical properties of the tissue (μ_a and μ_s') or the motion of blood cells within the probed volume of tissue. To estimate the relative sensitivity of τ_{exp} to changes in each of these factors, we calculated the dependence of τ_{exp} on μ_a and μ_s' for fixed values of BFI. We found a weak dependence of

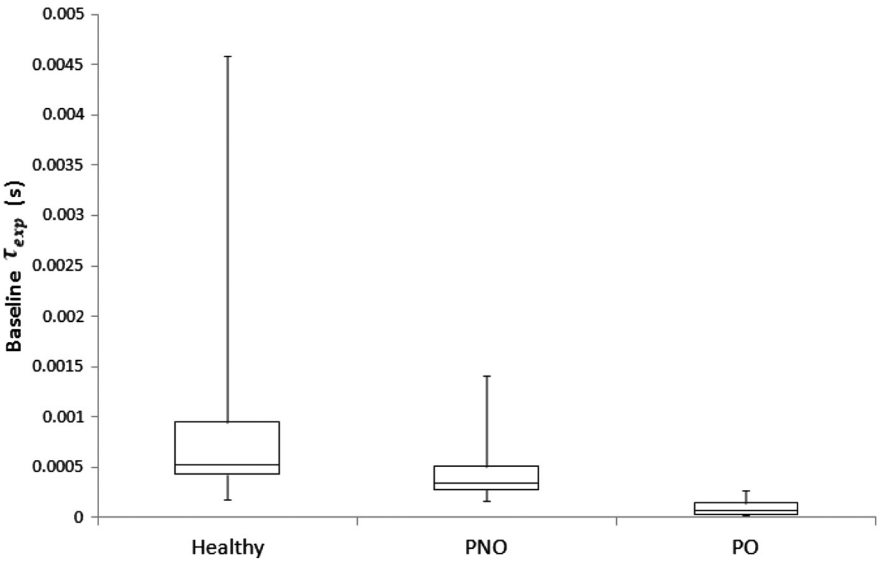

Fig. 4 Experimental $\tau_{\text{exp .baseline}}$ obtained during the all baseline measurement sessions for HSs ($n = 34$ measurement sessions), PNOs ($n = 28$), and POs ($n = 10$). The bottom bar represents the minimum while the top error bar is the maximum, the bottom line of the box represents the first quartile, top line of the box is the third quartile, and middle line is the median.

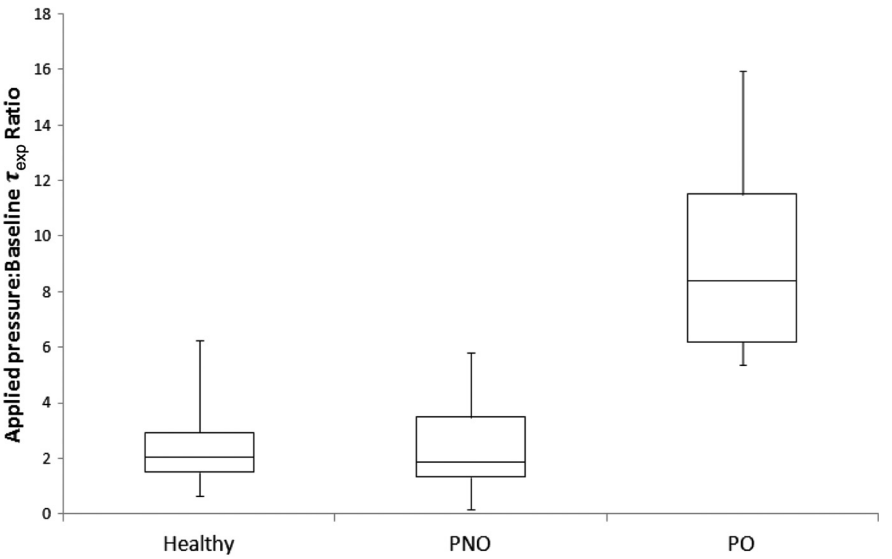

Fig. 5 The ratios of $\tau_{\text{exp .pressure}}$ obtained during applied pressure measurements to baseline $\tau_{\text{exp .baseline}}$ are shown on graphic. The data from all sessions for HSs ($n = 34$ measurement sessions), PNOs ($n = 28$), and POs ($n = 10$) are included in each of the boxes and whiskers. The bottom bar represents the minimum while the top error bar is the maximum, the bottom line of the box represents the first quartile, top line of the box is the third quartile, and middle line is the median. A 1-tailed *t*-test indicates a significant difference (5×10^{-7}) between PNO and PO subjects.

τ_{exp} on μ_a. Specifically, τ_{exp} changed by only 19% as values of μ_a ranged from 0.05 to 0.17 cm^{-1}, values that are typically seen in tissue. In principle, τ_{exp} shows a dependence on μ_s'. For example, τ_{exp} decreased by a factor of approximately 3 as values of μ_s' increased from 5 to 15 cm^{-1}, as shown in Fig. 6.

We observe from Fig. 4 that values of τ_{exp} during baseline measurements in PNOs were 2 to 3 times greater than those measured in POs. However, the average measured values of μ_s' in PNOs (10.3 cm^{-1}) were only slightly smaller than those measured in POs (11.0 cm^{-1}). This difference in μ_s' does not account for the much larger difference in τ_{exp}; therefore, we conclude that the observed differences in τ_{exp} are primarily attributable to differences in blood flow. Similarly, most of the observed 10 times increase of τ_{exp} in PO subjects between the baseline and applied pressure phases of our protocol can likely be attributed to changes in blood flow rather than changes in μ_s', since Table 2 shows that values of μ_s' only increased from 11.0 to 12.7 cm^{-1}.

The simulations reported in Fig. 6 were performed within the framework of an algorithm described previously.[34] We chose

Table 2 Mean (standard deviation) of absorption (μ_a) and reduced scattering coefficients (μ_s') for PNOs, POs, and silicone phantom measured at $\lambda = 830$ nm before each measurement session.

	μ_a (cm^{-1})			μ_s' (cm^{-1})		
	PNO	PO	Silicone phantom	PNO	PO	Silicone phantom
Baseline	0.078 (0.016)	0.078 (0.014)	0.11 (0.035)	10.3 (1.8)	11.0 (1.6)	11.2 (1.0)
Applied pressure	0.058 (0.015)	0.079 (0.012)		13.2 (3.3)	12.7 (2.7)	
Released pressure	0.070 (0.018)	0.086 (0.019)		11.3 (3.0)	11.4 (1.5)	

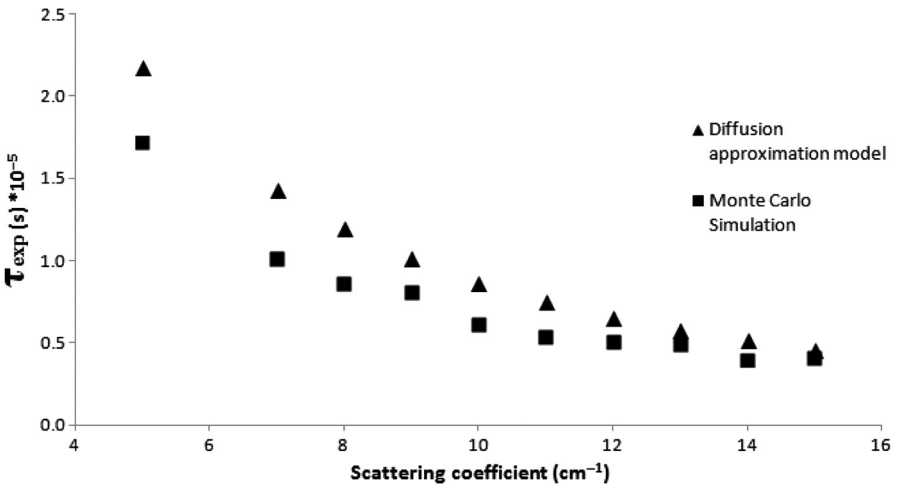

Fig. 6 Dependence of τ_{exp} on μ_s' for values 5 to 15 cm^{-1} calculated using the diffusion approximation model (triangles) and Monte Carlo simulation model (squares).

$\alpha D_b = 0.510^{-8}$ cm^2/s. To account for the temporal decay of the TCF, the weight of the n'th simulated photon was multiplied by the factor $\exp[-k^2\langle\Delta r^2(\tau)\rangle\mu_s' R_n/3]$, or for Brownian diffusion $\exp(-2\alpha D_B\tau\mu_s R\sum_j q_j^2)$,[32,38] where R and q_j are the random values of the optical path and wave transfer at the j-order of scattering, respectively; summing is performed over scattering orders.

We calculated BFI by fitting the experimental TCF using the Brownian model with D_B as the unknown parameter for the average experimental μ_a and μ_s' in each protocol stage.

The shift from baseline to released pressure shows a BFI that is systematically declining after every measurement session for all POs, as seen in Fig. 7 and Table 3. PO1 and PO2 both show BFI shifts that cross the x-axis, indicating that the average blood

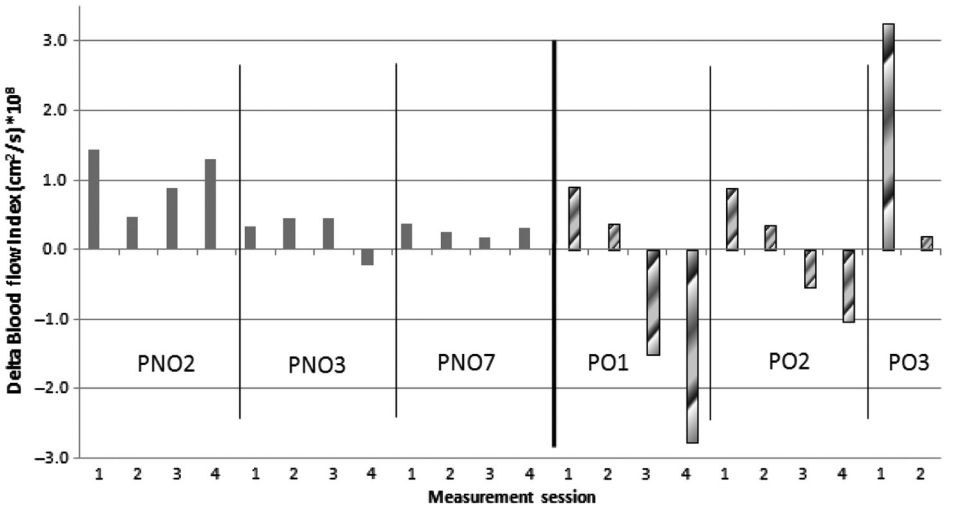

Fig. 7 Change in BFI between baseline and released pressure stages of the measurement protocol. POs (striped) exhibit a consistent drop in the magnitude of blood flow during the released pressure stage from day to day, while no specific pattern is observed in PNOs (solid). Only three PNOs are displayed because the same temporal trends are seen in all other PNOs.

Table 3 Slopes calculated using the change in BFI between baseline and released pressure stages during consecutive measurement sessions show a strong negative trend for all POs.

ID	Slope $\times 10^{-10}$
PNO1	7.7
PNO2	0.0
PNO3	−5.6
PNO4	−1.0
PNO5	−6.4
PNO6	−2.3
PNO7	−4.0
PNO8	−0.9
PO1	−39
PO2	−24
PO3	−153

flow during released pressure was lower than the average baseline blood flow, while PO3 showed a single large drop in BFI during released pressure before the wound opened the following day.

The released pressure stage, as the patient is moved from a load bearing position back to a lateral position, was of particular interest since it showed a temporal trend, which allowed further distinction between POs and PNOs. The systematic decrease for POs may further indicate a progression in the structural deterioration of the microvasculature from day to day until eventual ulceration. It is important to note that only two measurement sessions were performed on PO3 due to ulceration prior to the third session; the downward trend, however, is still apparent.

5 Discussion and Conclusions

In the future, it may be possible to use raw TCF data as a diagnostic tool for early detection of tissue injury that leads to open PIs. We can hypothesize that the capillary network is very sensitive to outside factors and lacks normal oxygen and nutrition supply for these patients. However, since we measured just three patients who developed an open ulcer, it is just a preliminary speculation.

DCS and DNIRS technologies have the potential to be used to assess the risk of advanced ulceration in patients with intact skin and nonblanchable redness. Throughout each of the stages of the protocol, τ_{exp} and BFI data could be used to distinguish between POs and PNOs within two weeks of recruitment.

Baseline measurements, which are more simple and do not require the use of a complicated experimental probe, showed a large difference between τ_{exp} for groups of medical patients, PO and PNO ($p = 0.005$). If our analysis of the relatively small influence of scattering coefficients on τ_{exp} is correct, we suppose that the blood flow is higher for POs patients, although they have similar redness on the skin surface. Solely monitoring baseline τ_{exp} can be useful in the prediction of PI development.

In healthy tissue, faster blood flow may be interpreted as a higher influx of nutrients and oxygen to the probed area; however, in patients with compromised circulation, increased blood flow does not necessarily reflect the tissue nutrition. Previous studies have demonstrated an increase in blood flow in diabetic patients during hypoxia and capillary ischemia of several organs, which may be caused by the microvascuature compensating for decreased nutritional status of local tissue.[44]

1. PO subjects exhibit a very high sensitivity of blood flow to the applied pressure. This conclusion follows from the large increase in τ_{exp} values during the applied pressure stage. Tissue and blood vessels with high sensitivity to applied body pressure may be the initial reason for PI development. These preliminary data suggest that it may be possible to predict open PIs in patients with low mobility by monitoring local blood flow.

   We expect that when patients are moved to the supine position, the pressure will compress the tissue, causing an increase in μ_s'. Further, τ_{exp} is expected to decrease as the microvasculature is compressed and blood flow slows. We observed a very large shift in TCF (in the direction of large τ) for PO subjects relative to PNO and HSs. In this case, it is reasonable to conclude that blood flow in PO patients slowed down more than in PNO and HSs.

   We can hypothesize that the capillary network in PO subjects is very sensitive to outside factors because it is damaged and may lack normal oxygen and nutrition supply, which may lead to their open PIs. A larger decrease in blood flow from baseline values to the applied pressure stage for POs may be indicative of a damaged or impaired microcirculation that is unable to sustain proper blood flow under the load of the patient's body. This result can be explained physiologically through shunting, which is a situation in which blood is efficiently diverted to where it is most needed due to changes in activity.[45] This phenomenon is achieved through the contraction of precapillary sphincters, which are bands of smooth muscle surrounding the origination of capillaries, to adjust the blood flow into the capillaries and/or direct the blood to a different area. It is possible that the POs were experiencing microvascular damage causing PI, which may cause the same effect as shunting in blood vessels since we see an increase in BFI for patients who develop advanced ulcers. However, since we have measured only three patients who developed an open ulcer, this is just a preliminary speculation.

2. We observed temporal trends between consecutive sessions in released pressure changes of BFI from baseline (Fig. 7) in POs that were not observed in PNO subjects. It may be difficult to use these types of measurements for diagnostic purposes since multiple measurements must be performed over a period of several days. However, these data may provide information about

the deterioration of local microvasculature in patients who are developing PIs beneath the skin's surface, if these trends are observed in a larger clinical trial.

Disclosures

No conflicts of interest, financial or otherwise, are declared by the authors.

Acknowledgments

This work was supported by the Office of the Assistant Secretary of Defense for Health Affairs, through the FY 2014 Spinal Cord Research Program under Award No. W81XWH-14-1-0614. Opinions, interpretations, conclusions, and recommendations are those of the author and are not necessarily endorsed by the Department of Defense. The U.S. Army Medical Research Acquisition Activity, Fort Detrick, Maryland is the awarding and administering acquisition office. The authors would like to thank the staff at the Magee Rehabilitation Hospital for their assistance and use of their facilities. A special thank you to Mr. Paul Buttner and Ms. Naoko Otsuji for their assistance throughout the study. Last, the authors would like to thank the Coulter-Drexel translational research partnership for their generous support of this project. V. Kuzmin acknowledges the partial support of the Russian Foundation for Basic Research, Grant No. 16-02-00465.

References

1. M. N. Kim et al., "Noninvasive measurement of cerebral blood flow and blood oxygenation using near-infrared and diffuse correlation spectroscopies in critically brain-injured adults," *Neurocrit. Care* **12**, 173–180 (2010).
2. Y. Hou et al., "Obstructive sleep apnea-hypopnea results in significant variations in cerebral hemodynamics detected by diffuse optical spectroscopies," *Physiol. Meas.* **35**, 2135–2148 (2014).
3. J. Li et al., "Noninvasive detection of functional brain activity with near-infrared diffusing-wave spectroscopy," *J. Biomed. Opt.* **10**, 044002 (2005).
4. T. Durduran et al., "Spatiotemporal quantification of cerebral blood flow during functional activation in rat somatosensory cortex using laser-speckle flowmetry," *J. Cereb. Blood Flow Metab.* **24**, 518–525 (2004).
5. F. Jaillon et al., "Activity of the human visual cortex measured non-invasively by diffusing-wave spectroscopy," *Opt. Express* **15**, 6643–6650 (2007).
6. J. Li et al., "Transient functional blood flow change in the human brain measured noninvasively by diffusing-wave spectroscopy," *Opt. Lett.* **33**, 2233–2235 (2008).
7. P.-Y. Lin et al., "Regional and hemispheric asymmetries of cerebral hemodynamic and oxygen metabolism in newborns," *Cereb. Cortex* **23**, 339–348 (2013).
8. D. R. Busch et al., "Continuous cerebral hemodynamic measurement during deep hypothermic circulatory arrest," *Biomed. Opt. Express* **7**, 3461–3470 (2016).
9. T. Durduran et al., "Optical measurement of cerebral hemodynamics and oxygen metabolism in neonates with congenital heart defects," *J. Biomed. Opt.* **15**, 037004 (2010).
10. E. M. Buckley et al., "Cerebral hemodynamics in preterm infants during positional intervention measured with diffuse correlation spectroscopy and transcranial Doppler ultrasound," *Opt. Express* **17**, 12571–12581 (2009).
11. N. Roche-Labarbe et al., "Near-infrared spectroscopy assessment of cerebral oxygen metabolism in the developing premature brain," *J. Cereb. Blood Flow Metab.* **32**, 481–488 (2012).
12. U. Sunar et al., "Monitoring photobleaching and hemodynamic responses to HPPH-mediated photodynamic therapy of head and neck cancer: a case report," *Opt. Express* **18**, 14969–14978 (2010).
13. U. Sunar et al., "Noninvasive diffuse optical measurement of blood flow and blood oxygenation for monitoring radiation therapy in patients with head and neck tumors: a pilot study," *J. Biomed. Opt.* **11**, 064021 (2006).
14. P. Farzam et al., "Noninvasive characterization of the healthy human manubrium using diffuse optical spectroscopies," *Physiol. Meas.* **35**, 1469–1497 (2014).
15. G. Yu et al., "Real-time in situ monitoring of human prostate photodynamic therapy with diffuse light," *Photochem. Photobiol.* **82**, 1279–1284 (2007).
16. C. Lindner et al., "Diffuse optical characterization of the healthy human thyroid tissue and two pathological case studies," *PLoS One* **11**, e0147851 (2016).
17. D. Rohrbach et al., "Photodynamic therapy-induced microvascular changes in a nonmelanoma skin cancer model assessed by photoacoustic microscopy and diffuse correlation spectroscopy," *Photonics* **3**, 48 (2016).
18. G. Ramirez et al., "Chemotherapeutic drug-specific alteration of microvascular blood flow in murine breast cancer as measured by diffuse correlation spectroscopy," *Biomed. Opt. Express* **7**, 3610 (2016).
19. T. L. Becker et al., "Monitoring blood flow responses during topical ALA-PDT," *Biomed. Opt. Express* **2**, 123–130 (2010).
20. U. Sunar et al., "Hemodynamic responses to antivascular therapy and ionizing radiation assessed by diffuse optical spectroscopies," *Opt. Express* **15**, 15507–15516 (2007).
21. G. Yu et al., "Noninvasive monitoring of murine tumor blood flow during and after photodynamic therapy provides early assessment of therapeutic efficacy," *Clin. Cancer Res.* **11**, 3543–3552 (2005).
22. E. S. Papazoglou et al., "Changes in optical properties of tissue during acute wound healing in an animal model," *J. Biomed. Opt.* **13**(4), 044005 (2008).
23. E. S. Papazoglou et al., "Noninvasive assessment of diabetic foot ulcers with diffuse photon wave methodology: pilot human study," *J. Biomed. Opt.* **14**(6), 064032 (2009).
24. M. S. Weingarten et al., "Diffuse near-infrared spectroscopy prediction of healing in diabetic foot ulcers: a human study and cost analysis," *Wound Repair Regen.* **20**, 911–917 (2012).
25. A. Stekelenburg et al., "Deep tissue injury: how deep is our understanding?" *Arch. Phys. Med. Rehabil.* **89**(7), 1410–1413 (2008).
26. "National Pressure Ulcer Advisory Panel (NPUAP) announces a change in terminology from pressure ulcer to pressure injury and updates the stages of pressure injury," Washington, DC (2016).
27. K. Balzer et al., "The Norton, Waterlow, Braden, and Care dependency Scales: comparing their validity when identifying patients' pressure sore risk," *J. Wound Ostomy Continence Nursing* **34**(4), 389–398 (2007).
28. N. Aoi et al., "Ultrasound assessment of deep tissue injury in pressure ulcers: possible prediction of pressure ulcer progression," *Plast. Reconstruct. Surg.* **124**(2), 540–550 (2009).
29. D. Judy et al., "Improving the detection of pressure ulcers using the TMI ImageMed System," *Adv. Skin Wound Care* **24**(1), 18–24 (2011).
30. D. A. Boas, L. E. Campbell, and A. G. Yodh, "Scattering and imaging with diffusing temporal field correlations," *Phys. Rev. Lett.* **75**(9), 1855–1858 (1995).
31. R. C. Haskell et al., "Boundary conditions for the diffusion equation in radiative transfer," *J. Opt. Soc. Am. A* **11**, 2727 (1994).
32. D. J. Pine et al., *Phys. Rev. Lett.* **60**(12), 1134–1137 (1988).
33. J. P. Culver et al., "Diffuse optical tomography of cerebral blood flow, oxygenation, and metabolism in rat during focal ischemia," *J. Cereb. Blood Flow Metab.* **23**(8), 911–924 (2003).
34. V. L. Kuzmin et al., "Diffuse photon density wave measurements and Monte Carlo simulations," *J. Biomed. Opt.* **20**(10), 105006 (2015).
35. B. J. Tromberg et al., "Non-invasive in vivo characterization of breast tumors using photon migration spectroscopy," *Neoplasia* **2**(1–2), 26–40 (2000).
36. I. Fridolin, K. Hansson, and L. G. Lindberg, "Optical non-invasive technique for vessel imaging: II. A simplified photon diffusion analysis," *Phys. Med. Biol.* **45**(12), 3779–3792 (2000).
37. G. H. Weiss, R. Nossal, and R. F. Bonner, "Statistics of penetration depth of photons re-emitted from irradiated tissue," *J. Mod. Opt.* **36**(3), 349–359 (1989).

38. G. Maret and P. E. Wolf, "Multiple light scattering from disordered media. The effect of Brownian motion of scatterers," *Z. Phys. B: Condens. Matter* **65**(4), 409–413 (1987).
39. Y. Shang et al., "Extraction of diffuse correlation spectroscopy flow index by integration of N-th-order linear model with Monte Carlo simulation," *Appl. Phys. Lett.* **104**, 193703 (2014).
40. T. Durduran et al., "Diffuse optics for tissue monitoring and tomography," *Rep. Prog. Phys.* **73**(7), 076701 (2010).
41. T. Binzoni and F. Martelli, "Assessing the reliability of diffuse correlation spectroscopy models on noise-free analytical Monte Carlo data," *Appl. Opt.* **54**(17), 5320 (2015).
42. D. A. Boas et al., "Establishing the diffuse correlation spectroscopy signal relationship with blood flow," *Neurophotonics* **3**(3), 031412 (2016).
43. T. H. Pham et al., "Broad bandwidth frequency domain instrument for quantitative tissue optical spectroscopy," *Rev. Sci. Instrum.* **71**(6), 2500–2513 (2000).
44. B. Fagrell, G. Jorneskog, and M. Intaglietta, "Disturbed microvascular reactivity and shunting—a major cause for diabetic complications," *Vasc. Med.* **4**(3), 125–127 (1999).
45. A. R. Pries et al., "The shunt problem: control of functional shunting in normal and tumour vasculature," *Nat. Rev. Cancer* **10**(8), 587–593 (2010).

Biographies for the authors are not available.